Optical Engineering

OpticalEngineering.SPIEDigitalLibrary.org

Image intensity recovery with mitigation in the presence of gamma–gamma atmospheric turbulence using encrypted chaos

Ali Mohamed
Monish R. Chatterjee

SPIE.

Ali Mohamed, Monish R. Chatterjee, "Image intensity recovery with mitigation in the presence of gamma–gamma atmospheric turbulence using encrypted chaos," *Opt. Eng.* **58**(3), 036110 (2019), doi: 10.1117/1.OE.58.3.036110.

Image intensity recovery with mitigation in the presence of gamma–gamma atmospheric turbulence using encrypted chaos

Ali Mohamed and Monish R. Chatterjee*
University of Dayton, Department of Electrical and Computer Engineering, Dayton, Ohio, United States

Abstract. Mitigation of image distortion under modified von Karman-type phase turbulence has been examined by using acousto-optic (A-O) chaos waves generated via feedback in a Bragg cell. The chaos wave transferred to the optical carrier either over an image-bearing transparency (with the image reconstructed with appropriate lensing), or alternatively the two-dimensional image (both static as well as dynamic) is embedded in the chaos wave and propagated over the turbulent layer. These investigations demonstrate that the properties of chaos waves including relative immunity from variations in the propagation path enable reduction or mitigation of the image distortion under turbulent conditions. Mitigation of image distortion is explored using propagation through a turbulent atmospheric layer characterized by gamma–gamma type intensity fluctuations. Standard weak, moderate, and strong turbulence conditions are applied for the numerical analysis based on the corresponding structure parameters. Following standard approach, the relevant probability density functions are generated using small- and large-scale eddies (α and β numbers) incorporated into the turbulence model. In addition, mitigation of image distortion due to gamma–gamma turbulence is examined for propagation along a low-altitude slanted path with a fixed slope and different elevation angles using A-O chaos along with the Huffnagel–Valley model. Stationary images are transmitted under nonchaotic and chaotic conditions, and the corresponding distortions in the received images are measured using the conventional metric of bit error rates. The system performances under nonchaotic and chaotic transmissions are compared with the intent to establish that packaging a signal within a chaos wave offers a degree of distortion mitigation.
[DOI: 10.1117/1.OE.58.3.036110]

Keywords: turbulence; image encryption; acousto-optic chaos; gamma–gamma turbulence; turbulent and chaotic propagation.

Paper 181637 received Nov. 19, 2018; accepted for publication Mar. 12, 2019; published online Mar. 26, 2019.

1 Introduction

Free-space optics (FSO) is an optical wireless line-of-sight communication system offering optical bandwidth connections with security, electromagnetic (EM) interference invulnerability, free spectrum usage, and low power utilization without requiring physical fiber-optic cable.[1] FSO has speed comparable to the optical fiber (potentially multigigabits per sec level), implying it will not slow down the optical data rate. It can be considered an alternative to the optical fiber for the "last mile" problem when fiber optic links are unavailable or are too expensive to implement.

However, the channel FSO transmitter usually faces atmospheric turbulence. Significant challenges may arise for FSO transmission from increased scintillation and other fluctuations in atmospheric turbulence channels. Optical irradiance (especially for coherent sources) suffers random fluctuations of amplitude and phase when the channel refractive index is distorted by time-varying temperature and pressure.[2,3]

A variety of turbulence models are typically used to describe the probability density functions (pdf) statistics of the irradiance fluctuations. The models log-normal, gamma–gamma, and negative exponential are used for weak, weak to strong, and saturation regimes, respectively. The work presented here is limited to gamma–gamma turbulence model applied to turbulence of varying strengths. The gamma–gamma distribution can describe the atmospheric fluctuation caused by weak-to-strong turbulence. This model combines the small- and large-scale scattering elements as multiplicative components of a fading phenomenon, resulting in a fairly accurate modeling of a turbulent FSO channel in the moderate-to-strong regime.[4] The present research is motivated by recent success in exploring turbulence mitigation for signal and image transmission through turbulent atmospheres represented by the modified von Karman-type (MVKS) model via the use of chaotic encryption.[5,6] It was conjectured recently that propagation of a chaotic wave through turbulence may offer some invulnerability that would make the propagated signal relatively undisturbed by the impacts of turbulence in the medium.[5–8]

The problem was set up by generating a gamma–gamma process representing turbulent fluctuations. In the modeling used, a modulated binary phase shift keying (BPSK) image is propagated via a strategy that uses spectral analysis for the propagation of a modulated EM wave through the turbulence. The input EM wave may be treated as a modulated optical carrier represented as a sinusoidal phasor with a slowly time varying envelope (denoted SVEA under phasor domain analysis) arising from the (time-dependent, nonsinusoidal) information signal. It turns out that the transmitted BPSK modulated image may be encrypted by a chaotic carrier and a similar approach applied. In this case, a heterodyne

*Address all correspondence to Monish R. Chatterjee, E-mail: mchatterjee1@udayton.edu

0091-3286/2019/$25.00

strategy is needed at the receiver for recovery of the information encrypted on the chaos after propagation through the turbulence.[9] In practice, EM propagation is more likely to be slanted relative to the horizontal plane (or the ground level). While purely horizontal propagation does occur in a lot of cases, for measuring the signals or images propagated through turbulence, physical setups often involve a receiver at a higher elevation compared with the source (such as in cases involving imaging platforms on hilltops, or even airborne machines). Therefore, for any such slanted propagation, it is necessary to examine the consequence of variable turbulence parameters (such as the space-dependent structure and Fried parameters that depend on the physical altitude of the point of interest along the actual propagation path) on the transmitted signal or image. Any diffractive analysis would therefore have to take into account this altitude-dependence for greater accuracy.[10] An appropriate physical model that incorporates altitude dependence is the Huffnagel–Valley (HV) turbulence profile. The organization of this paper is as follows. In Sec. 2, we briefly preview acousto-optic (A-O) chaos and its properties. An overview of gamma–gamma turbulence and related modeling are outlined in Sec. 3. Numerical simulations and results for the propagation of modulated (chaotic and nonchaotic) EM waves through gamma–gamma atmospheric turbulence under different conditions are reported in some detail in Sec. 4. Finally, concluding remarks and ideas for further extensions of the research are presented in Sec. 5.

2 Acousto-Optic (A-O) Chaos and Chaos Generation

As stated previously,[5] considering signals that include static images undergo adverse effects in the presence of atmospheric turbulence (modeled by using gamma–gamma here), different techniques are adopted in order to mitigate the distortions in the recovered signal *a priori* or postprocessing.

Some well-known processes involve digital and alternative modes of postprocessing whereby the distorted information is restored to some degree via use of corrective filters and different processing strategies;[11–13] our approach, however, involves preprocessing whereby the distortion of the signal or information is mitigated pre-emptively before the signal suffers any significant degradation. To this end, it was speculated earlier[7] that the inherent immutability and robustness of signals securely transmitted via encrypted chaotic modulation may consequently provide some immunity to the propagation and recovery of a signal transmitted over turbulence as well. An early effort in this method held out the promise that this strategy may likely be effective.[5,14–16]

Subsequently, the transmission process has been extended to include slanted paths (implying anisoplanaticism) as well as different elevation angles, the results for which are presented in this paper. Note that examinations relative to turbulence mitigation under unslanted or horizontal propagation have been reported in earlier work.[17] Accordingly, in what follows, we briefly review the phenomena of A-O diffraction and in particular, the generation of RF chaos waves within the feedback loop of a Bragg cell. In the Bragg regime, the incident light is diffracted into the zeroth- and first-orders (intensities I_0 and I_1), where I_1 represents upshifted diffraction. The resulting first order is picked up by a linear photo detector at the output, amplified and then fed back to the adder in the feedback loop. The adder adds the feedback with the dc bias input ($\tilde{\alpha}_0$) and feeds it to the RF source that generates the RF input, which is then incident on the Bragg cell via a transducer.[9] Such a (nonlinear) A-O feedback device is described as hybrid (hence termed HAOF) in nature since both RF and optical effects are combined. The standard Bragg cell transmitter with feedback is shown in Fig. 1.

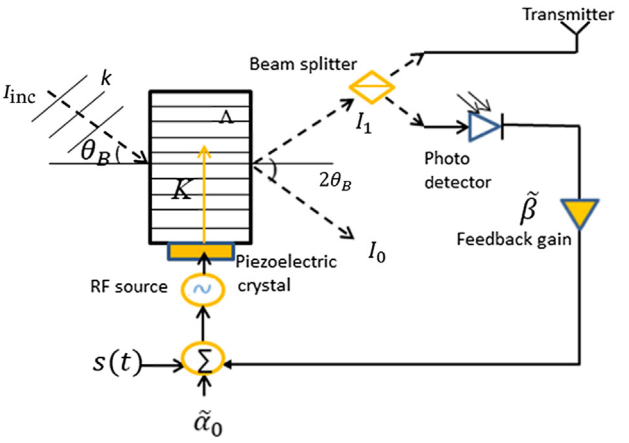

Fig. 1 A-O modulator with first-order feedback in the Bragg regime.

Note that $s(t)$ in the figure represents a possible *ac* (message) signal, which may be added to the RF bias circuit. The corresponding first-order detected intensity follows the nonlinear dynamical equation (based on uniform plane wave optics):

$$I_1(t) = I_{\text{inc}} \sin^2\left[\frac{1}{2}(\tilde{\alpha}_0(t) + \tilde{\beta} I_1(t - TD))\right], \tag{1}$$

where $\tilde{\beta}$ is the effective feedback gain, I_{inc} is the incident intensity, $\tilde{\alpha}_0$ is the peak phase delay, and TD is the feedback time delay including photo detector conversion delay. The states of the HAOF system investigated via its nonlinear dynamics (NLD) is controlled by specific threshold values of the parameters $\tilde{\alpha}_0$, $\tilde{\beta}$, TD, and I_{inc}. By changing the effective bias input ($\tilde{\alpha}_{0,\text{eff}}$) from 0 to 4 and TD around 1 ms, a series of NLD, and so-called bifurcation maps may be generated. Note that the highly sensitive behavior of this (quadratic map) system may be thoroughly examined by numerically examining the closed loop system of Eq. (1) or its discrete equivalent by varying the *key* parameters in different combinations. When there is a gradual increase in the value of $\tilde{\beta}$ from 2, there exists a nominal threshold value of 2.41 such that following transitions from monostable, bistable, and multistable states, the system enters full-blown chaos as shown in the bubble in Fig. 2.

Incidentally, the threshold value of $\tilde{\beta}$ may actually be lowered by altering one or more of the other dynamical parameters, especially I_{inc}. Both $\tilde{\beta}$ and $\tilde{\alpha}_0$ play crucial roles in determining the dynamics of the HAOF system. The process of chaotic encryption of a data signal can be mathematically described as approximately similar to amplitude modulation (AM). For the process of encryption, the precise passband of $\tilde{\alpha}_0$ which would allow the intensity of the first-order light beam to be in chaos within the band has to be identified.

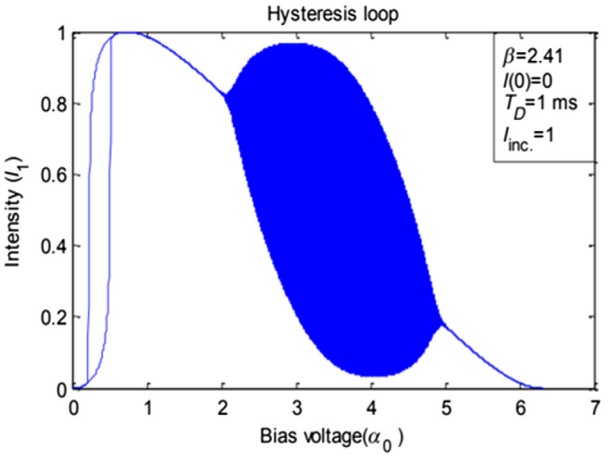

Fig. 2 Formation of hysteresis loop for chaotic case.

The chaos generated is randomly oscillatory versus time with the average period approximately $1/(2\text{x}TD)$.

The center of the $\tilde{\alpha}_{\text{total}}$ (which is the combination of the bias and signal inputs to the RF circuit) passband is set at the bias voltage level $\hat{\alpha}_{0,\text{bias}}$. When this dc value is added with the intended message signal, $s(t)$, the overall value should be within the bounds of the available passband on the bifurcation map.[18] The overall bias input may be written as

$$\tilde{\alpha}_{\text{total}} = \tilde{\alpha}_0 + s(t). \tag{2}$$

The effective first-order PD current (representing the amplitude of the first-order light) with the HAOF in chaos (in the presence of a message signal) can be written as follows:

$$I_1(t) = I_{\text{inc}} \sin^2\left\{\frac{1}{2}[\tilde{\alpha}_{\text{total}}(t) + \tilde{\beta} I_1(t - TD)]\right\}. \tag{3}$$

Note that in Eq. (3), $\tilde{\alpha}_{\text{total}}(t)$ replaces $\tilde{\alpha}_0$ in Eq. (1) because of the addition of an AC signal $s(t)$ to the summer in the feedback loop. Incidentally, $\tilde{\alpha}_0$ is essentially a DC bias voltage applied to the bias input of the RF driver. The encrypted first-order light beam under chaos modulation is transmitted from the HAOF device via a beam splitter and it propagates over a turbulent atmospheric channel in free space. At the receiver end, to decode the encrypted message signal a coherent (heterodyne) receiver configuration is needed in order to extract the information from the encrypted chaos, as shown schematically in Fig. 3. In the figure, at the receiver end, the photodetector current is split into two paths, one in the RF feedback loop, and the other in the branch connecting to the multiplier in the demodulator path. The two fractions γ and δ add up to 1. Note that recovery of the signal from the chaos wave depends critically on the matching keys between the transmitter and receiver Bragg cells. This aspect provides an additional measure of security for the transmitted signal as has been studied extensively without the presence of turbulence.[14,16,18]

3 Gamma–Gamma Turbulence Model

Common turbulence models are the log-normal model (including Kolmogorov and MVKS models for weak to moderate turbulence regimes), K-distributed model (typically for strong turbulence regimes), and gamma–gamma model (applicable from weak to strong turbulence regimes).[19] The gamma–gamma statistics is found to describe FSO scintillation phenomena in a broad range of turbulence conditions. This model, proposed by Andrews et al.,[20,21] is based on the modulation process where the fluctuation of light radiation traversing a turbulent atmosphere is assumed to consist of small-scale (scattering, described by an α parameter) and large-scale (refraction, described by a β parameter) effects. It must be noted that small- and large-scale turbulence eddies are also represented in the MVKS and other models as l and L, which are measured as distances in meters. The α and β parameters in gamma–gamma on the other hand are dimensionless. In this work, a gamma–gamma random variable with a pdf is used to model the optical irradiance I as follows:

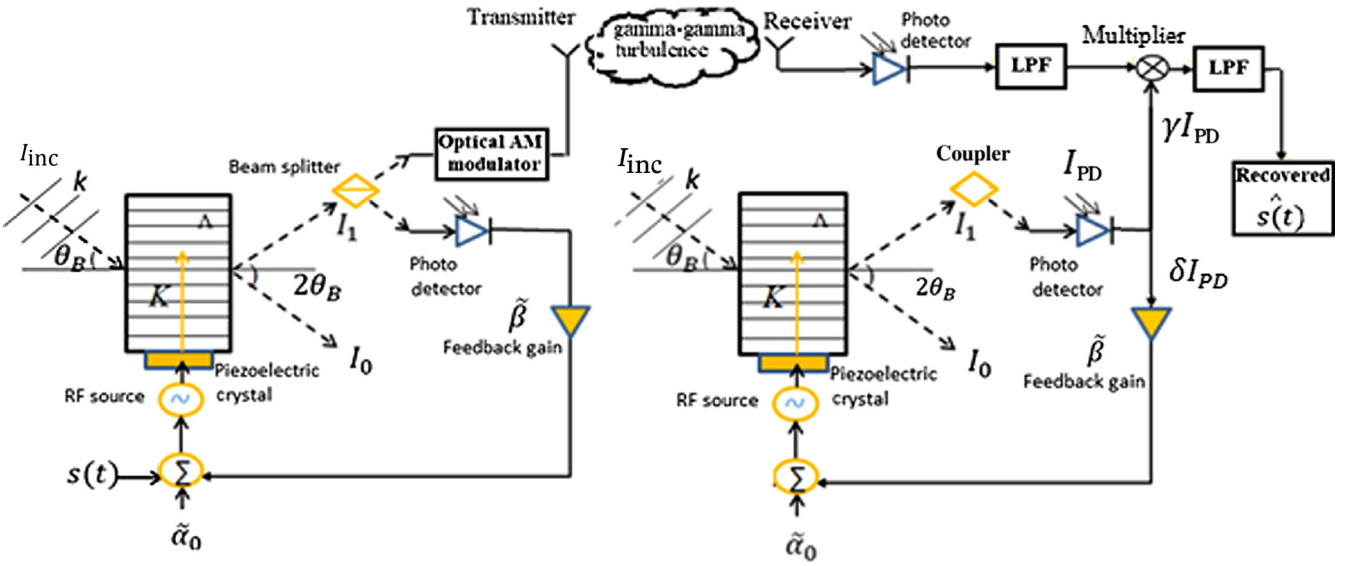

Fig. 3 HAOF transmitter and receiver pair.

$$f(I) = \frac{2(\alpha\beta)^{\frac{\alpha+\beta}{2}}}{\Gamma(\alpha)\Gamma(\beta)} I^{\left(\frac{\alpha+\beta}{2}\right)-1} K_{\alpha-\beta}\left(2\sqrt{\alpha\beta I}\right), \quad I > 0, \tag{4}$$

where the so-called shape parameters α and β, respectively, represent effective (dimensionless) numbers representing large- and small-scale eddies of the scattering process, as discussed earlier; additionally, $K_n(.)$ is the modified Bessel function of the second kind of order n, and $\Gamma(\cdot)$ represents the gamma function. The two parameters α and β characterizing the irradiance fluctuation pdf are related to the atmospheric conditions by Refs. 22 and 23 as follows, assuming the optical radiation at the receiver is a plane wave:

$$\alpha = \left\{ \exp\left[\frac{0.49\sigma_l^2}{\left(1 + 1.11\sigma_l^{\frac{12}{5}}\right)^{\frac{7}{6}}} \right] - 1 \right\}^{-1} \tag{5a}$$

and

$$\beta = \left\{ \exp\left[\frac{0.51\sigma_l^2}{\left(1 + 0.69\sigma_l^{\frac{12}{5}}\right)^{\frac{5}{6}}} \right] - 1 \right\}^{-1}, \tag{5b}$$

where α and β are functions of the Rytov variance σ_l^2. In addition, σ_l^2 is proportional to the atmospheric structure parameter C_n^2, which reflects the degree or strength of turbulence. Figure 4 shows the gamma–gamma pdf for three different turbulence regimes, namely, weak, moderate, and strong.

The plot shows that as the turbulence increases from the weak to the strong regime, we observe that when the strength of turbulence becomes strong, the gamma–gamma distribution approaches a negative exponential distribution.[22] We note that the gamma–gamma becomes more asymmetrical as the turbulence strength increases; this obviously changes both the mean and variance of the distributions. It can be shown (Fig. 5) that α is a convex function of σ_l^2 (reaching a minimum and subsequently curving upward), and β is a monotonically decreasing function. In addition, the relationship $\alpha > \beta$ always holds, and the smaller shape parameter β is lower bounded above 1 as σ_l^2 approaches ∞. These properties are borne out by the figure; note that as a consequence β does not decay to zero.

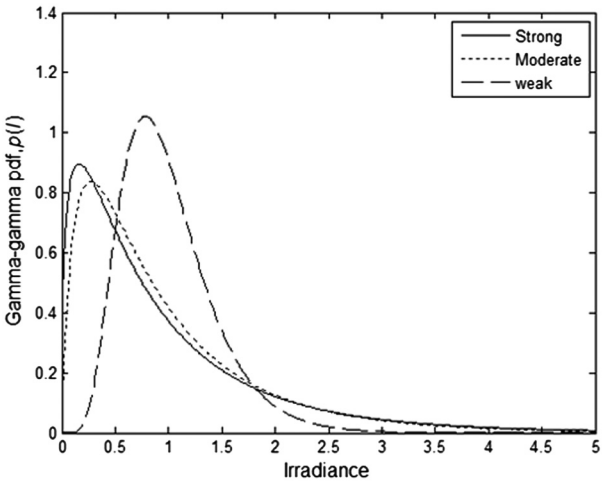

Fig. 4 Gamma–gamma pdf for three different turbulence regimes, namely, weak, moderate, and strong.

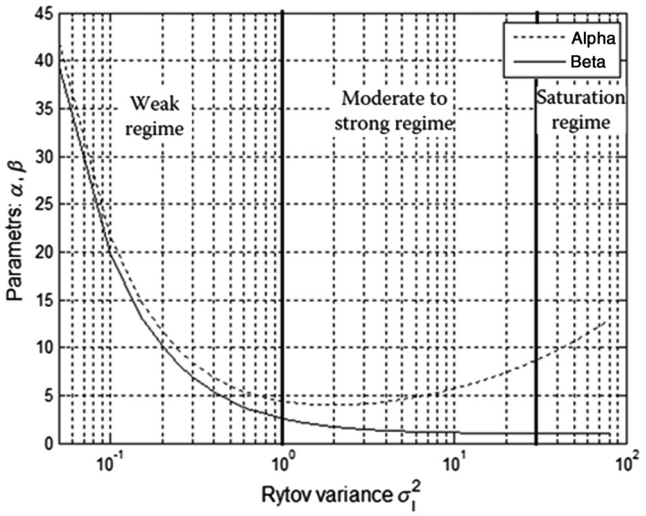

Fig. 5 Values of α and β under different turbulence regimes, namely, weak, moderate to strong, and saturation.

The average error rate over an atmospheric turbulence channel can be expressed as

$$P_e = \int_0^\infty p_e(I) f(I) \mathrm{d}I. \tag{6}$$

In Eq. (6) above, note that (for BPSK), the conditional error rate $p_e(I)$ is given by $p_e(I) = Q(\sqrt{\gamma I})$, where γ denotes the average SNR and $Q(.)$ is the Gaussian Q-function defined as $Q(x) = \int_x^\infty (e^{-\frac{t^2}{2}}/\sqrt{2\pi})\mathrm{d}t$. Using $p_e(I)$ and the gamma–gamma distribution [Eq. (4)], the unconditional bit error rate (BER) [from Eq. (6)] then becomes

$$P_e = \int_0^\infty Q\left(\sqrt{\gamma I}\right) \frac{2(\alpha\beta)^{\frac{\alpha+\beta}{2}}}{\Gamma(\alpha)\Gamma(\beta)} I^{\left(\frac{\alpha+\beta}{2}\right)-1} K_{\alpha-\beta}\left(2\sqrt{\alpha\beta I}\right)\mathrm{d}I. \tag{7}$$

The BER (related typically to $1/P_e$) can only be evaluated numerically from Eq. (7) as it does not have a closed-form solution.

Most of the earlier work by this group was focused on using the modified von Karman power spectral density (MVKS). It turns out that the MVKS model applies particularly well to turbulence environments that are relatively low-altitude and also have weak to moderate structure parameters. The motivation to examining the gamma–gamma model arises from the latter's adaptability to a broader range of turbulence strengths and also variable altitudes.

The generation of a gamma–gamma process requires the multiplication of two gamma distributions. These distributions maybe derived from a gamma process as[24]

$$x_{k+1} = \frac{x_k\tau_c + \alpha\theta\Delta t + \frac{\theta\Delta t(\xi_k^2 - 1)}{2} + [2x_k\theta\tau_c\Delta t]^{1/2}\xi_k}{\Delta t + \tau_c}, \tag{8}$$

where indexes k and $k+1$ are related to the values of the signal amplitude at times t_k and t_{k+1}, respectively, Δt is the

sampling time, ξ_k are samples of the white Gaussian noise process, and τ_c is the correlation time. By substitution of $\theta = 1/\alpha$ *for* x_k and $\theta = 1/\beta$ *for* y_k into the gamma–gamma process, the resulting intensity, I_k, is simply the multiplication of the solutions of the above two gamma processes; hence,

$$I_k = x_k y_k. \tag{9}$$

4 Image Propagation Through Gamma–Gamma Turbulence Without and With A-O Chaos

In this section, we report on numerical simulations of image transmission and retrieval using a plane EM wave via two approaches: (1) digitizing the two-dimensional (2-D) transparency (or image) function using pixels encoded into PCM data, and thereby transmitting the binary data by BPSK modulation. The BPSK-modulated signal is transmitted over a gamma–gamma turbulence channel for different values of the Rytov variance. Finally, the image is recovered and reconstructed using photodetection and D/A conversion with thresholding; and (2) alternatively, the BPSK image is encrypted onto a chaotic carrier before being transmitted over a gamma–gamma channel under similar turbulence conditions. In the results presented later, the performances relative to the two approaches are examined and compared. Once again the two cases are examined under a low-altitude slanted path with a fixed propagation distance (with variable slope).

In what follows, the propagation of nonchaotic and chaotic (BPSK) signals through gamma–gamma atmospheric turbulence and their characteristics at the receiver are presented in some detail. This investigation is necessary to enable performance comparisons vis-à-vis turbulence mitigation when chaotic modulation/encryption is applied in place of standard nonchaotic carrier modulation. A standard amplitude-modulated EM wave may be expressed as

$$E_{AM}(x,y,z,t) = E_0(x,y,z)[1 + ms(t)]\cos(\omega_0 t - kz), \tag{10}$$

where m is the modulation index and $s(t)$ is the modulating BPSK (message) signal, and $E_0(x,y,z)$ is a Gaussian-profiled envelope. We note here that, unlike the Gaussian profile beam used for transmission through turbulence as described above, the chaos wave generated from the A-O Bragg cell arises from a uniform plane wave profile at the input of the HAOF device.

In a standard nonchaotic scenario, the modulated Gaussian-profiled optical carrier is first detected through a photodetector and thereafter the message signal is recovered via appropriate filtering. We next note that if the optical carrier has an envelope containing an RF-modulated carrier (such as an encrypted chaos wave obtained from an HAOF device), recovery would require additional use of heterodyne AM demodulation followed by filtering. The above is clearly understood by noting a mathematical representation of a modulated chaotic wave through the Bragg cell may be expressed as[9,17]

$$s_{\mathrm{ch}}(t) = A_C[1 + ms(t)]\cos(\omega_{ch} t), \tag{11}$$

where m is the modulation index, ω_{ch} is an equivalent (average) chaos frequency, A_C is the carrier amplitude, and $s(t)$ is the signal that modulates the chaos wave. Note that $s_{\mathrm{ch}}(t)$ in Eq. (11) becomes the modulating signal for the optical carrier modulation implied in Eq. (10). As mentioned, the time-dependent chaos wave generated is approximately amplitude modulated when the signal wave is applied via the RF (sound) input. We note that the chaotic waveform in Eq. (11) is essentially RF in nature and manifests itself in the feedback loop as a current in the PD. The modulated optical wave at the output of the Bragg cell may therefore be approximately written as (assuming AM/envelope modulation)

$$E_{AM}(x,y,z,t) = E_0(x,y,z)[1 + \tilde{m}s_{\mathrm{ch}}(t)]\cos(\omega_0 t - kz), \tag{12}$$

where $\tilde{m}$ is the optical modulation index. Also, we may apply SVEA-type approximation because the optical carrier is orders of magnitude faster than either the chaotic or the signal waveforms and likewise the carrier amplitude is higher than that of the signal. As described, a message waveform is therefore embedded onto the chaotic carrier at the output of a Bragg cell. The resulting numerical data for the encrypted chaos wave are used to amplitude-modulate the optical carrier. It must be noted that for the case where information is used to directly modulate the optical carrier, photodetection automatically transfers the intensity corresponding to the envelope, and the optical carrier is eliminated. Thereafter, signal recovery involves simple electronic processing. For the case of a chaotic envelope riding the optical carrier, however, photodetection will at first result in a scaled version of the modulated chaos to be detected via the photocurrent. Subsequently, a heterodyne receiver strategy with appropriate cut-off frequency is used to retrieve the digitized baseband (message) signal.

4.1 *Isoplanatic Propagation of Nonchaotic and Chaotic EM Waves Through Turbulence*

The gamma–gamma turbulence was generated by choosing the values of α, β, and σ_l^2 that fall in the required turbulence region (see Fig. 5). Next, the process was generated by use of Eqs. (8) and (9) for three turbulence strengths (Table 1); this is presented in Fig. 6.

Note that the correlation time $\tau_c = 20$ ms, with the sampling time $\Delta t = 10^{-4}$ s. In all scenarios, the propagation distance is set to $L_T = 2.6$ km. The PDF of the generated process for strong turbulence versus the theoretical [Eq. (4)] is shown in Fig. 7. The solid (CW) curve arises from use of Eq. (4) wherein the PDF is expressed mathematically; on the other hand, the stacked histogram in the figure comes from the use of the time data derived from Eqs. (8) and (9), expressing the signal irradiance $I(t)$ versus time (see Fig. 6). Thereafter, Matlab is used to generate the probability

Table 1 Turbulence parameters.

Parameter	Weak	Moderate	Strong
σ_l^2	0.2	1.6	3.5
α	11.6	4.0	4.2
β	10.1	1.9	1.4

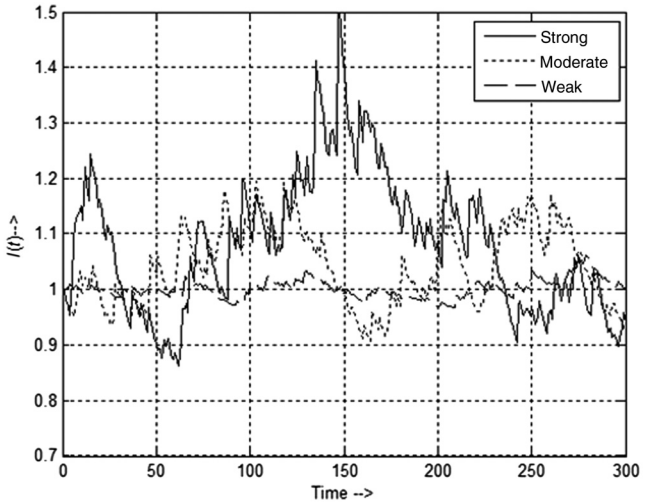

Fig. 6 Gamma–gamma process for weak, moderate, and strong turbulence.

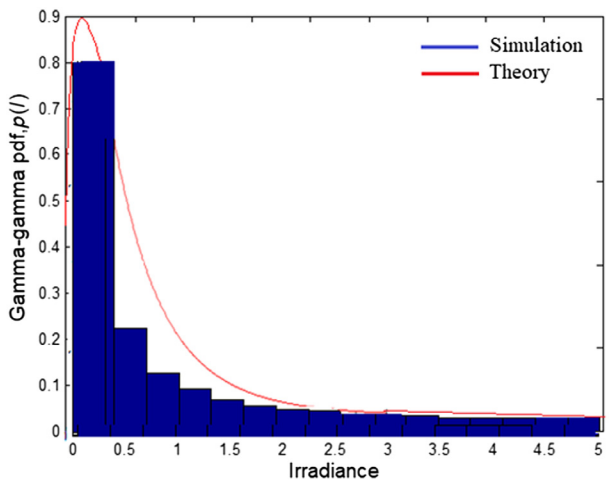

Fig. 7 The PDF of the generated gamma–gamma process and its theoretical plot for strong turbulence.

histogram shown in Fig. 7. As for the signal irradiance (along the horizontal axis in Fig. 7), it must be noted that every photodetector (and especially so for the one used to detect the EM output from the turbulent region in Fig. 3) in the communication system has a large enough aperture to capture the power across the incident light beam. We also note that even though the histogram appears to follow the shape of the probability curve, the two not entirely overlapping. This "error" between the two graphs may be minimized increasing the amount of successive time data collected in the Matlab computation. Similar derivations are carried out for the weak and moderate cases as well.

The digitized image corresponding to the firemen pattern[25] converted to pixelated grey scale values (PCM is used for encoding through the Matlab routine) and its BPSK version are shown in Figs. 8(a) and 8(b), respectively.

The BPSK-modulated signal (chaotic and nonchaotic) is transmitted over the gamma–gamma fading channel with different values of the Rytov variance (see Table 1). The resulting reconstructed/decoded images under nonchaotic condition for different turbulence strengths are shown in Fig. 9.

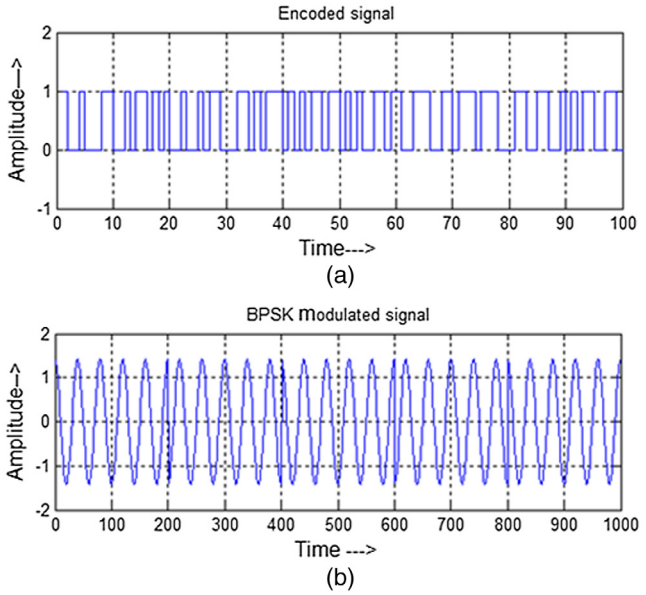

Fig. 8 (a) PCM encoded signal and (b) BPSK-modulated signal.

The results show that stronger turbulence leads to higher distortion (with a noisy "snowflake" effect) in the recovered image. Thus, weak turbulence displays minimal image distortion, whereas moderate turbulence displays limited image distortion or fuzziness. Next, we examine the propagation of a modulated chaotic wave through the same turbulent environment (weak, moderate, and strong). The encrypted chaotic image signal is shown in Fig. 10(a). From the reconstructed images [shown for the three turbulence cases in Figs. 10(b)–10(d)], it appears visually that the chaotic transmission maintains greater image integrity against turbulence, and thereby offers turbulence mitigation. For comparison, Fig. 11 shows the BER curve for the A-O chaotic BPSK system alongside the curve for a nonchaotic BPSK system.

The BER curves (expressed as probability of error P_e) in Fig. 11 are obtained as follows. For either the nonchaotic or chaotic recovered image, we obtain using Matlab a peak SNR value computed between the original and the recovered images, denoted as γ in Eq. (7). Thereafter, the BER is computed using Eq. (7). The data along the SNR axis are generated by varying the input signal power levels and recomputing the γ values to generate the corresponding BERs.

Quantitatively, measuring the P_es at 10^{-8} across the SNR axis leads to signal to noise improvements of about 0.55 dB under strong turbulence, 1.1 dB for moderate, and 2 dB under weak turbulence. Therefore, to achieve a fixed BER performance, less signal power is needed under chaotic transmission compared with nonchaotic. The results clearly indicate a consistent improvement in the system performance vis-à-vis turbulence mitigation under the entire range of turbulence strengths tested. We find from these calculations that under the assumed turbulence strengths, the recovered image SNR improvements are in the range 14% to 60% (the lowest being for the strong turbulence case). Incidentally, the BPSK digital modulation scheme was chosen for the source image simply because, in general, this provides superior noise performance compared with most of the common alternative schemes, such as ASK or FSK.

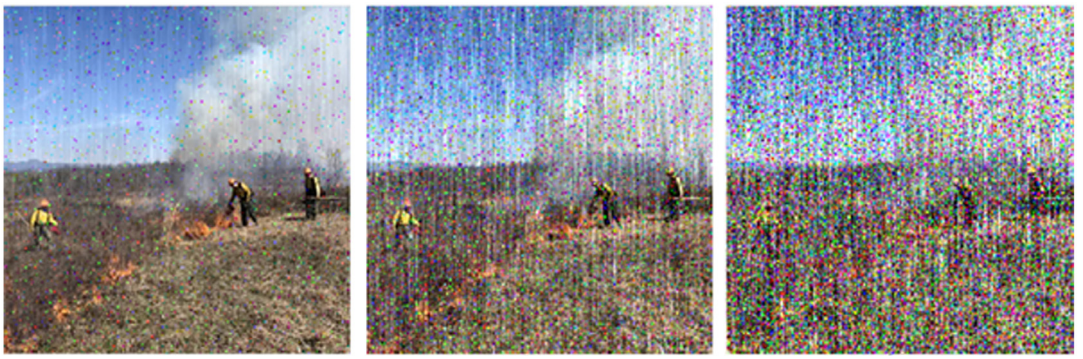

(a) (b) (c)

Fig. 9 Simulator output under nonchaotic propagation; turbulence condition (a) weak, (b) moderate, and (c) strong.

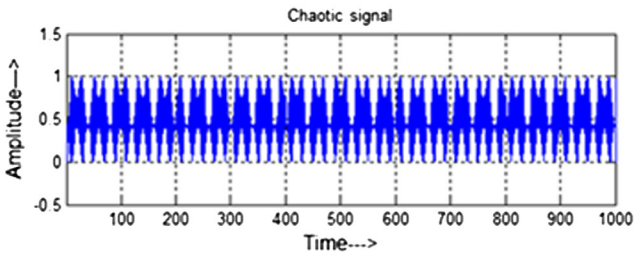

(a)

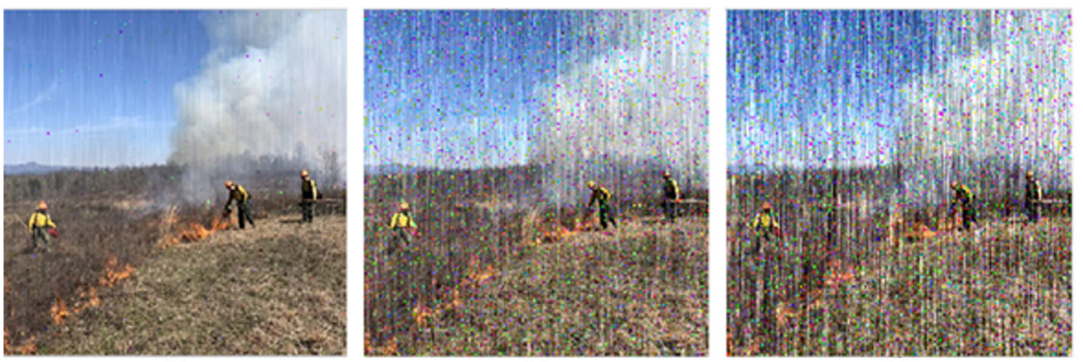

(b) (c) (d)

Fig. 10 Simulator output under chaotic propagation. (a) The encrypted chaotic image signal, (b–d) reconstructed images under turbulence condition weak, moderate, and strong, respectively.

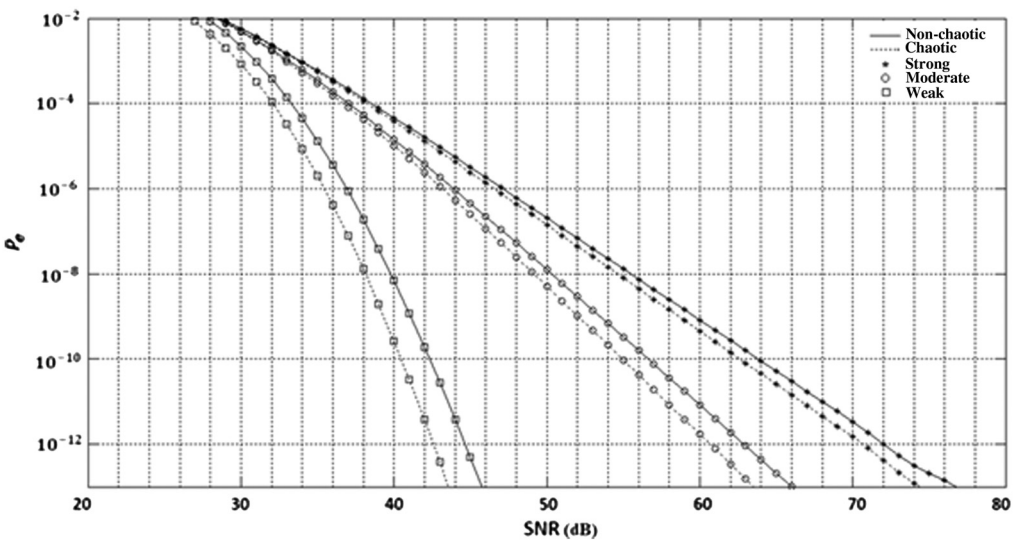

Fig. 11 BERs for chaotic versus nonchaotic propagation over different turbulent strength gamma–gamma channels.

4.2 *Anisoplanatic Propagation of Nonchaotic and Chaotic EM Wave Through Turbulence*

In this section, we report on numerical simulations of imaging using a plane EM wave via the same approaches as before. The primary difference is that the performances relative to the two approaches are examined and compared under a slanted path. We note that when the HV (not discussed here; see Refs. 5 and 10) is applied to the slanted path, the computed equivalent C_n^2 for three elevation angles 30 deg, 8 deg, and 2 deg fall in the weak, moderate, and strong turbulence range, respectively, with values $C_n^2 = 3 \times 10^{-16}$ m$^{-2/3}$, $C_n^2 = 1.76 \times 10^{-15}$ m$^{-2/3}$, and $C_n^2 = 1 \times 10^{-14}$ m$^{-2/3}$. Incidentally, the HV model is based on near-ground turbulence effects whereby the turbulence is intrinsically stronger at lower altitudes. Hence, when the propagation path has a lower slant angle, the field experiences higher effective turbulence along the total path. Therefore, in order to numerically simulate a gamma–gamma process for the different elevation angles, a separate set of calculations is needed. First, an equivalent C_n^2 is plugged into this equation ($\sigma_l^2 = 1.23 C_n^2 k^{7/6} L_T^{11/6}$),[22] where k is the wave number and L_T is the propagation distance, whence an equivalent σ_l^2 is computed in conjunction with Eqs. 5(a) and 5(b). The resulting values of α and β are listed in Table 2. The propagation distance is fixed at an L_T of 7 km. The gamma–gamma process was generated by applying Eqs. (8) and (9) for the three turbulence strengths.

The BER curves (expressed as probability of error P_e) shown in Fig. 12 are obtained as described before. The recovered image SNR improvements are in the range 10% to 60%, corresponding to 0.4 and 2.0 dB SNR improvements (the lowest being for the 2 deg turbulence case).

Table 2 Turbulence parameters under different elevation angles.

Parameter	$\theta = 30$ deg	$\theta = 8$ deg	$\theta = 2$ deg
σ_l^2	0.22	1.31	4.8
α	10.76	4.13	4.53
β	9.25	2.14	1.24

5 Conclusions

The problem of EM signal propagation through turbulence with different strengths has been examined for the gamma–gamma type of turbulence statistics. This work partly builds on recent work involving signal transmission (including 2-D images and videos) through the MVKS turbulence environment, specifically for isoplanatic as well as anisoplanatic propagation paths whereby the resulting damaging effects of the turbulence on the retrieved signal/image have been studied, and methods of mitigation of the damages proposed. One such mitigation strategy involves the use of chaotic carrier waves upon which the message signal is encrypted either as analog information or as digitally encoded bit streams. For the current gamma–gamma model, the problem is broadly divided into two regimes, namely, a horizontal (or isoplanatic) propagation case and also one involving slanted paths (anisoplanatic), such that the results are obtained for weak, moderate, and strong turbulence conditions (described via the structure parameter and the related Rytov variance) under both nonchaotic and chaotic conditions. The results consistently indicate that the use of chaotic carriers offer measurable mitigation and recovered signal improvement for all conditions. It turns out that the effectiveness of the chaotic transmission in mitigating signal damage, however, decreases for stronger turbulence (0.55 dB margin of improvement compared with 2 dB for weak, for example, for the horizontal propagation problem). For the problem of slanted propagation, the HV model for lower atmospheric propagation indicates that the effective turbulence is stronger at shallow propagation compared with steeper propagation paths. As a result, it is found that even though chaotic encryption consistently improves turbulence mitigation, the margin of improvement is higher for larger slant angles (steeper paths) compared with lower angles (shallower paths). Incidentally, newer work by other research groups appears to utilize chaos waves for turbulence mitigation

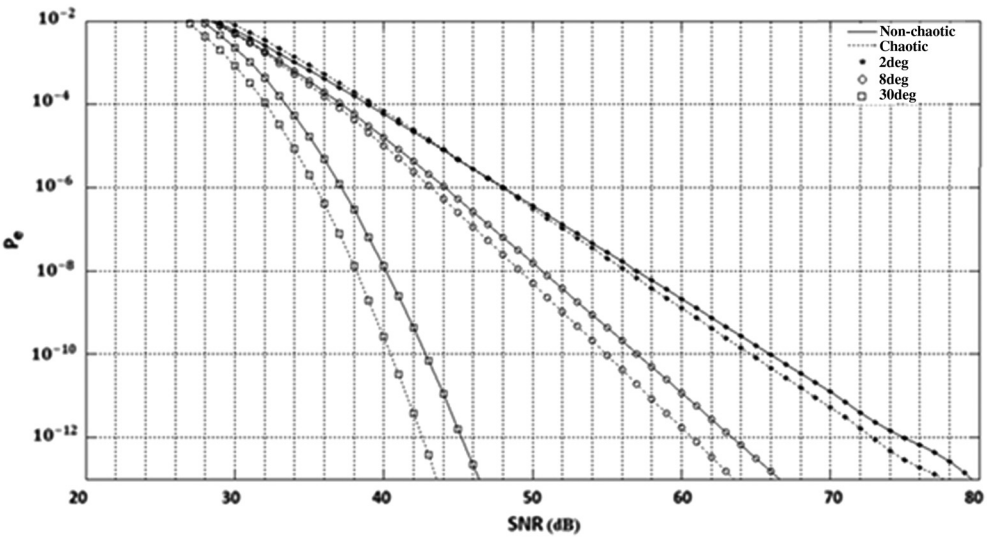

Fig. 12 BERs for chaotic versus nonchaotic propagation over different turbulent strength gamma–gamma channels.

wherein some of the current series of results are cited.[26] Further efforts to improve (stronger) turbulence mitigation using chaotic and related strategies are currently under investigation. We also note that this paper is an extended elucidation of related work that was presented at the SPIE Defense and Security Conference in Orlando, Florida, in April, 2018. Details of the related paper may be found in Ref. 27. One final note regarding channel based pre- and postprocessing: since FSO is the means of propagation here, only the gamma–gamma turbulence model is used to characterize the channel, and no pre- or postprocessing (including digital image processing strategies) relative to the channel has been applied. Indeed, packaging a signal in chaos and subsequent recovery of the signal from the encrypted chaos comprise preprocessing and postprocessing for this system and this approach has been compared with the nonchaotic case consistently in this paper.

References

1. K. Kiasaleh, "Performance analysis of free-space on-off-keying optical communication systems impaired by turbulence," *Proc. SPIE* **4635**, 150–161 (2002).
2. X. Zhu and J. M. Kahn, "Free-space optical communication through atmospheric turbulence channels," *IEEE Trans. Commun.* **50**(8), 1293–1300 (2002).
3. J. Li and M. Uysal, "Achievable information rate for outdoor free space optical," in *IEEE Global Telecommun. Conf.*, Vol. 5, pp. 2654–2658 (2003).
4. M. A. Al-Habash, L. C. Andrews, and R. L. Phillips, "Mathematical model for the irradiance probability density function of a laser beam propagating through turbulent media," *Opt. Eng.* **40**(8), 1554–1562 (2001).
5. M. R. Chatterjee and A. Mohamed, "Anisoplanatic image propagation along a slanted path under lower atmosphere phase turbulence in the presence of encrypted chaos," *Proc. SPIE* **10204**, 102040G (2017).
6. A. Mohamed and M. R. Chatterjee, "Non-chaotic and chaotic propagation of stationary and dynamic images through MVKS turbulence," revised and submitted to J. Mod. Opt. for publication.
7. A. K. Majumdar, Department of the Navy, China Lake, CA, Private communication.
8. A. Mohamed and M. R. Chatterjee, "Chaos-based mitigation of image distortion under anisoplanatic electromagnetic signal propagation through turbulence," in *Frontiers in Optics*, Washington, DC, pp. JW4A.1 (2017).
9. M. R. Chatterjee and M. Alsaedi, "Examination of chaotic signal encryption and recovery for secure communication using hybrid acousto-optic feedback," *Opt. Eng.* **50**(5), 055002 (2011).
10. J. Power, "Modeling anisoplanatic effects from atmospheric turbulence across slanted optical paths in imagery," Master's Thesis, University of Dayton (2016).
11. S.-T. Chen and M. R. Chatterjee, "A numerical analysis and expository interpretation of the diffraction of light by ultrasonic waves in the Bragg and Raman-Nath regimes multiple scattering theory," *IEEE Trans. Educ.* **39**(1), 56–68 (1996).
12. A. Korpel and T.-C. Poon, "Explicit formalism for acousto-optic multiple plane-wave scattering," *J. Opt. Soc. Am.* **70**, 817–820 (1980).
13. M. R. Chatterjee, T.-C. Poon, and D. N. Sitter Jr., "Transfer function formalism for strong acousto-optic Bragg diffraction of light beams with arbitrary profiles," *Acustica* **71**(2), 81–92 (1990).
14. F. S. Almehmadi and M. R. Chatterjee, "Improved performance of analog and digital acousto-optic modulation with feedback under profiled beam propagation for secure communication using chaos," *Opt. Eng.* **53**, 126102 (2014).
15. F. S. Almehmadi and M. R. Chatterjee, "Secure chaotic transmission of electrocardiography signals with acousto-optic modulation under profiled beam propagation," *Appl. Opt.* **54**(2), 195–203 (2015).
16. F. S. Almehmadi, "Secure chaotic transmission of digital and analog signals under profiled beam propagation in acousto-optic Bragg cells with feedback," Doctoral Dissertation, University of Dayton (2015).
17. M. R. Chatterjee and F. Mohamed, "Diffractive propagation and recovery of modulated (including chaotic) electromagnetic waves through uniform atmosphere and modified von Karman phase turbulence," *Proc. SPIE* **9833**, 98330F (2016).
18. S. K. Chaparala, "Secure encryption and decryption by aperture variations of a photodetector in an acousto-optic Bragg cell," Master's Thesis, University of Dayton (2016).
19. M. Niu et al., "Performance analysis of coherent wireless optical communications with atmospheric turbulence," *Opt. Exp.* **20**(6), 6515–6520 (2012).
20. I. Andrea, "Free space optics links affected by optical turbulence: channel modeling, measurements and coding techniques for error mitigation," Doctoral Dissertation, The University of Palermo (2013).
21. L. C. Andrews, R. L. Phillips, and C. Y. Hopen, *Laser Beam Scintillation with Applications*, SPIE, Bellingham, Washington (2001).
22. Z. Ghassemlooy, W. Popoola, and S. Rajbhandari, *Optical Wireless Communications System and Channel Modeling with Matlab*, CRC Press, Boca Raton, Florida (2012).
23. W. O. Popoola, Z. Ghassemlooy, and E. Leitgeb, "Free-space optical communication using subcarrier modulation in gamma–gamma atmospheric turbulence," in *9th Int. Conf. Transparent Opt. Networks (ICTON '07)*, Warsaw, Poland, Vol. 3, pp. 156–160 (2007).
24. D. Bykhovsky, "Simple Generation of gamma, gamma–gamma, and K distributions with exponential autocorrelation function," *J. Light. Technol.* **34**(14), 2106–2110 (2016).
25. "Prescribed fire at Sumter National Forest. Burning to maintain the grasslands," https://imgur.com/gallery/PkN54 (11 March 2018).
26. M. M. Sepantaie, N. M. Namazi, and A. M. Sepantaie, "Spectral analysis and implementation of secure chaotic free-space optical communication systems," *Opt. Eng.* **57**(10), 106101 (2018).
27. M. R. Chatterjee and A. Mohamed, "Mitigation of image intensity distortion using chaos-modulated image propagation through gamma-gamma atmospheric turbulence," *Proc. SPIE* **10650**, 106500E (2018).

Ali Mohamed received his BSEE degree in communication engineering from Sabha University, Sabha, Libya, in 1999, and his MSEE degree from the University of Colorado, Denver, in 2011. He is currently completing his PhD at the University of Dayton, Dayton, Ohio, USA. His areas of research interests include atmospheric turbulence, image processing, communication, and digital signal processing.

Monish R. Chatterjee has been a professor of electrical and computer engineering (ECE) at the University of Dayton since 2002. He has authored over 75 papers in archival journals and conference proceedings, several book chapters, four literary books, numerous literary essays, and presented over 125 papers at international conferences. He is a senior member of the IEEE, OSA, SPIE, and a fellow of the Golden Key National Honors Society.